Author/s:
Cadusch, JJ;Meng, J;Wen, D;Shrestha, VR;Crozier, KB

Title:
Compact, Lightweight, and Filter-Free: An All-Si Microspectrometer Chip for Visible Light Spectroscopy

Date:
2022-02-16

Citation:
Cadusch, J. J., Meng, J., Wen, D., Shrestha, V. R. & Crozier, K. B. (2022). Compact, Lightweight, and Filter-Free: An All-Si Microspectrometer Chip for Visible Light Spectroscopy. ACS Photonics, 9 (2), pp.474-481. https://doi.org/10.1021/acsphotonics.1c01187.

Persistent Link:
https://hdl.handle.net/11343/332923

Compact, Light-Weight and Filter-Free: An All-Si Microspectrometer Chip for Visible Light Spectroscopy

Journal:	*ACS Photonics*
Manuscript ID	ph-2021-01187r.R2
Manuscript Type:	Article
Date Submitted by the Author:	n/a
Complete List of Authors:	Cadusch, Jasper; The University of Melbourne, Department of Electrical and Electronic Engineering Meng, Jiajun; The University of Melbourne, Department of Electrical and Electronic Engineering Wen, Dandan; University of Melbourne , Department of Electrical and Electronic Engineering Shrestha, Vivek; The University of Melbourne, School of Physics Crozier, Kenneth; University of Melbourne, School of Physics

Compact, Light-Weight and Filter-Free: An All-Si Microspectrometer Chip for Visible Light Spectroscopy

Jasper J. Cadusch[†,1], Jiajun Meng[1,2,3], Dandan Wen[1,4], Vivek Raj Shrestha[2], & Kenneth B. Crozier[,1,2,3]*

1 Department of Electrical and Electronic Engineering, The University of Melbourne, Parkville, Victoria 3010, Australia.

2 School of Physics, The University of Melbourne, Parkville, Victoria 3010, Australia.

3 Australian Research Council (ARC) Centre of Excellence for Transformative Meta-Optical Systems (TMOS), University of Melbourne, Parkville, Victoria 3010, Australia.

4 Shaanxi Key Laboratory of Optical Information Technology, School of Physical Science and Technology, Northwestern Polytechnical University, Xi'an 710129, China

ABSTRACT

Spectroscopic optical measurements of visible light provide important real-time information in many research and industrial settings. Conventional spectrometers are well established in this context due to their accuracy and reliability, however they have not found widespread use in field-deployed applications due to their bulk (size and weight) and susceptibility to mechanical shock. Here we demonstrate a compact, lightweight microspectrometer chip-scale solution based upon doped silicon nanophotonic elements, known as waveguide array (WGA) pixels. Each pixel is an array of 2.7 μm tall vertically oriented slab waveguides with a subwavelength array period, etched into a P-I-N doped silicon substrate. By adjusting the nanometric dimensions of each element we imbue our pixels with a structural color and each pixel's responsivity spectrum with distinct features. In doing this we forgo the need for the optical elements, such as gratings or interferometers, that one would normally need for a spectrometer. This opens the possibility for dramatic miniaturization and for improvements in mechanical robustness. We fabricate

and characterize 144 WGA pixels and use supervised machine learning techniques to perform spectroscopic measurements, including on biological samples, with our 6 mm x 6.5 mm chip. We find that our structurally-colored microspectrometer chip offers performance comparable to that of commercial spectrometer, making it well suited to field deployment in hand-held devices.

KEYWORDS: microspectrometers, waveguides, reconstructive spectroscopy, photodetectors, nanofabrication

INTRODUCTION

Medical diagnostics, chemical classification, industrial and environmental monitoring, and scientific research all use spectral information. Typically this is measured by instruments such as grating spectrographs and Fourier transform infrared (FTIR) spectrometers,[1] which combine precisely aligned conventional optical elements such as diffraction gratings or Michelson interferometers with a photodetector or with photodetector arrays. While this work well for many applications, there is currently a trend toward miniaturized optical systems. Indeed, research has recently focused on methods to reduce the weight and size of spectrometers, to better suit the emerging needs of hand-held consumer electronics, sensor networks that are part of the Internet-of-Things, and remote sensing platforms such as un-crewed aerial vehicles (UAVs). Developments in both machine learning and nanophotonics have driven these recent microspectrometer designs, with solutions falling into two camps: the planar filter-array detector-array (FADA) system or the filter-free chip-scale system.[2, 3] Both types rely upon spectral reconstruction via an algorithm as opposed to direct intensity read-out or fast Fourier transform. Prior art in FADA microspectrometer designs include thin film interference and plasmonic filters[4, 5], colloidal quantum dot absorptive filters incorporated onto charge coupled devices,[6] photonic crystals filters coupled to CMOS sensors,[7] and mid-infrared plasmonic filters designed to operate with microbolometer arrays.[8, 9, 10, 11] Filter-free microspectrometers on the other hand combine the spectral filtering component and the photo-

detecting component that all spectrometers require into a single element. This has been achieved by either spatially varying the chemical composition of semiconductor nanowires to alter the energy bandgap along the nanowire[12], or by creating a set of photodetectors with structural color, which arises due to optical resonances within the nanostructured element.[13, 14, 15, 16] Our microspectrometer presented here is of the latter type. Previous examples of structurally colored photodetectors include silicon or germanium nanowire arrays with transparent conducting top contacts made of indium tin oxide (ITO)[17] or graphene,[18] including a recent silicon nanowire microspectrometer chip with 24 vertical nanowire pixels.[13] An alternate structurally colored silicon-based example is a microspectrometer using a set of 20 fishnet photodetector pixels which do not require an additional transparent conducting top contact.[14]

Our chip, which we denote FIN144, consists 144 waveguide array (WGA) pixels. Each WGA is an array of vertically oriented slab waveguides, each of width s and period Λ. The geometric parameters (s,Λ) take sub- or near-wavelength values. Symmetric optical modes, both transverse magnetic (TM) and transverse electric (TE), are supported by the vertical waveguide arrays and can be excited directly by normally incident plane waves, without the need for additional momentum matching elements such as gratings or prisms.[19] The WGA are formed by inductively coupled reactive ion etching to the n+ layer of a P-I-N-I-P doped silicon substrate. Figure 1a shows a schematic of a WGA detector pixel, with the silicon doping indicated by color. Electrical contacts are made to the top p+ layer and to the n+ layer, forming a vertical P-I-N photodiode, with a responsivity spectrum dictated by the absorption that occurs within the lightly doped (n-) intrinsic region for the optical modes supported by the WGA. In each pixel, the spectral filtering and photon detection functions (which are needed in any spectrometer) occur within the same nanophotonic element, allowing for a large reduction in size compared to conventional grating spectrometers. Each WGA is connected to a pad mesa, a 100 μm x 100 μm x 2.7 μm (LxWxH) block of unetched silicon, contiguous with each waveguide, that allows us to form the top contact with each pixel and forgoes the need for planarization or a transparent conductive layer. Our chip design consists of 144 WGA pixels, organized into a 12 x 12 array, where each row of 12 pixels share a common electrical back

contact (the $n+$ layer) and each column of 12 pixels share a common top contact (the upper $p+$ layer connected via aluminum wires). Each pixel is 200 μm from its nearest neighbor. We term this configuration as 'row-and-column addressing'. It allows us to use many more pixels than the number of pins on our chosen chip carrier. By biasing one row and one column at a time, we can measure the photocurrent from an individual WGA pixel. Figure 1b shows a cross-sectional schematic of pixels in rows 1 and 2 and column 1 of FIN144. To electronically isolate the contact rows from one another, trenches are etched through the $n+$ layer and the lower intrinsic layer (thickness: 4 μm) into the lower $p+$ layer. We note that this design could be alternatively implemented using a P-I-N doped silicon-on-insulator substrate instead of the P-I-N-I-P substrate.

Following fabrication, which is detailed in the Methods section below, each WGA pixel is characterized by recording its responsivity spectra for TE and TM polarized illumination. Once the pixel responsivity library is recorded, FIN144 is used to measure both narrow and broadband test spectra. This is accomplished by measuring the photocurrents from each pixel created by the unknown spectrum and passing those 144 values to a supervised machine learning algorithm to estimate the unknown spectrum, given the known responsivity of each pixel. We demonstrate that the performance of FIN144 compares favorably with our much larger commercial spectrometer, even for test spectra comprising light transmitted through a bamboo leaf. We demonstrate that the FIN144 device can be used to measure changes in these spectra as the leaf ages over the course of a week. We conclude this paper with a summary of key results and possible applications.

RESULTS AND DISCUSSION

The nanofabrication steps used to realize the FIN144 microspectrometer chip are outlined in the Methods section below. The 144 WGA pixels have waveguide widths ranging from 150 nm to 200 nm in steps of 10 nm and array periods from 300 nm to 587.5 nm is steps of 12.5 nm. Figure 1c shows a scanning electron micrograph (SEM) of an example WGA pixel with geometric parameters (s=180 nm, Λ=425 nm) and the

attached pad mesa. In the inset image we see that the waveguide sidewalls are smooth and vertical, which is important for the optical properties of the pixel, reducing scattering losses and ensuring a well-defined set of waveguide modes.[20] Figure 1d shows an optical micrograph of one quadrant of FIN144, containing mostly yellow, orange and red pixels. Here the SU-8 bridges connect the WGA pixels of each column, allowing allows each column interconnect wire to span the 6.7 µm deep trenches separating the pixel rows. Figure 1e is an optical micrograph of a single WGA pixel, showing the pad mesa and the column interconnect wire carried atop the SU-8 bridges. The active area of the WGA pixel is the 100 µm x 100 µm red region to the right of the pad mesa. Note that the Al column wire makes direct (ohmic) contact with the top p+ layer of the pad mesa. To allow this, the Al_2O_3 surface passivation layer under the wire's track is removed prior to metallization. A photograph of the entire FIN144 chip prior to wire bonding, including row pads (left) and column pads (right) and their electrical isolation trenches, is provided as Figure 1f. In this image, each bright square comprises diffracted light from a WGA pixel. The chip has an extent of 6 mm x 6.5 mm, which is mostly due to the space required for our row-and-column implementation.

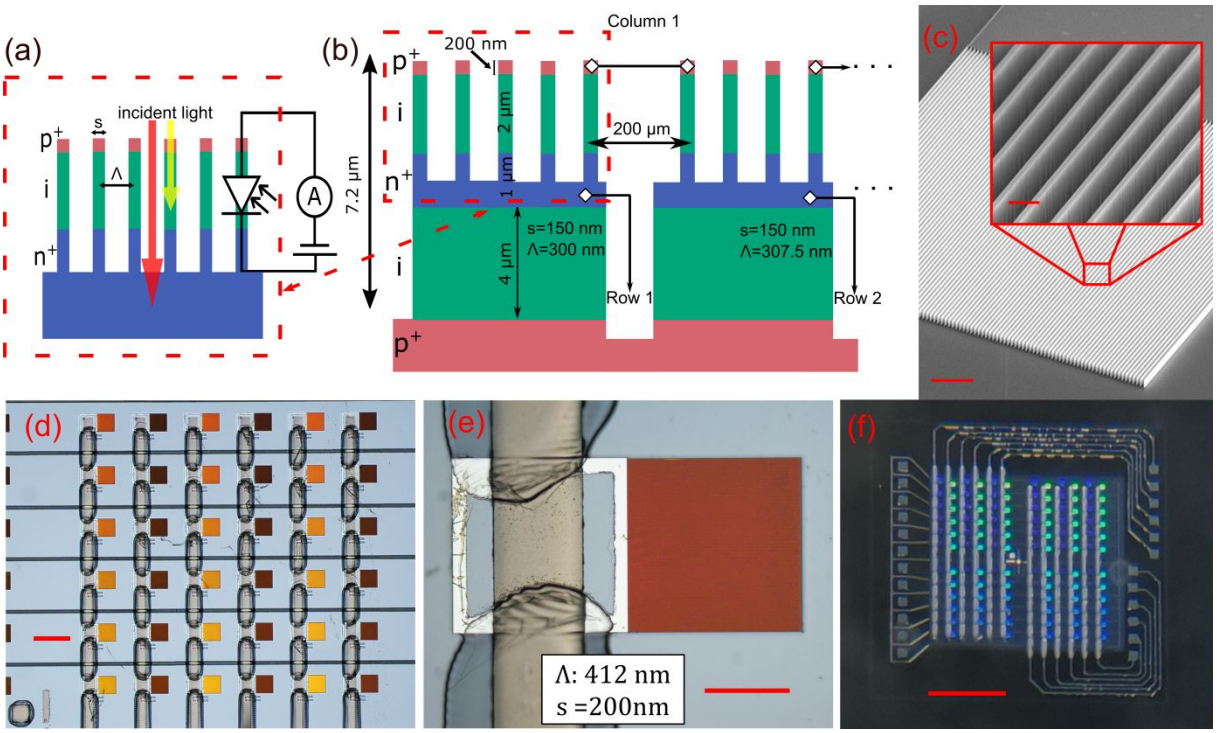

Figure 1. (a) Schematic of WGA pixel, with p+, i(n−) and n+-doped regions shown in red, green and blue, respectively. **(b)** Cross-sectional schematic of two WGA pixels (pixel row 1 and 2) within the same electrically connected column of FIN144 **(c)** SEM of a WGA pixel (scale bar: 17 μm). Inset: zoom-in of WGA (scale bar: 0.5 μm). **(d)** Optical micrograph of upper right quadrant of FIN144, showing WGA pixels, pad mesas, row trenches and SU-8 column bridges (scale bar: 200 μm). **(e)** Optical micrograph of WGA pixel and column wire after metallization (scale bar: 50 μm). **(f)** Photograph of FIN144 microspectrometer chip prior to packaging and wire-bonding (scale bar: 1500 μm).

After packaging FIN144 in a 28-pin dual in-line package and wire bonding it, we perform electrical and photonic characterization. We first measure the current-voltage (*I-V*) curves for each pixel on the chip. This is done with no illumination (i.e. dark), with TE-polarized illumination (power: 18 μW, λ = 560 nm) and with TM-polarized illumination (power: 18 μW, λ = 560 nm). Figure 2a shows the *I-V* curves for the WGA pixel with geometric parameters (s=180 nm, Λ=425 nm). In the inset, we provide a schematic defining TE and TM polarizations. It can be seen that the I-V curves exhibit the rectifying behavior that one would expect from P-I-N photodiodes, with a reverse saturation dark current of ~30 pA. When FIN144 is illuminated (at power: 18 μW, λ = 560 nm), the current is ~1 μA, which represents a ~10^5-fold increase over the dark current at -1V bias. At zero bias voltage the light on:off current ratio is around 10^6. We also note that the open-circuit voltage shifts by +0.7V when the pixel is illuminated. For this pixel, TM polarized light at λ=560 nm produces 1.7x the photocurrent of the TE polarized case. This difference in general depends on the values of s, Λ and λ. Figure 2b shows the measured external quantum efficiency (EQE) spectrum for this WGA pixel for both TE and TM polarizations measured under -4.8 V reverse bias. It can be seen that the EQE reaches as high as 0.55, which is achieved at λ=515 nm for TE light. The TM spectrum shows dual-moded behavior with peaks at λ=528 nm and λ=647 nm, with the EQE exceeding 0.38 for both. These EQE values surpass our previous reports[13, 14]. It has been reported that the internal quantum efficiency of nanostructured silicon PIN photodiodes can be improved by the addition of an ALD Al_2O_3 passivation layer.[21] It might be the case that the improvement in efficiency we obtain in this work might originate from this, although we do not verify this by control experiments. Figure 2c and 2d show the normalized EQE for 10 WGA pixels of fixed width (s=180 nm) and varied period, for TM- and TE-polarized illumination, respectively. Here two TM modes (TM2 and TM4) and one TE mode

(TE4) are apparent, as is the red-shift in peak EQE wavelength with increasing array period. Importantly, we see that there are spectral peaks across the visible range and into the near-infrared. Previously demonstrated microspectrometers based on structurally-colored photodetectors, where spectral filtering and electrical signal generation occur within the same photonic element, have relied upon a two stacked-detector configuration to expand their operating wavelength range beyond 600 nm into the near-infrared.[13, 14] The measured normalized EQE spectra for the remaining pixels can be found in the Supporting Information. Figure 2e shows measured responsivity spectra for the same WGA pixels and polarization as Figure 2c, with each successive curve offset by 0.17 A/W. These pixels have peak responsivities up to 0.25 A/W and the gradual change in peak position for both modes (TM2 and TM4) with increasing array period can be seen. To gain physical insight into this, one can analytically model a WGA as a high-contrast grating (HCG). The TE mode cut-off wavelengths, λ_c, can be calculated by solving Equation 1:

$$n_{Si}\tan\left(\frac{\pi n_{Si} s}{\lambda_c}\right) = \tan\left(\frac{\pi(\Lambda - s)}{\lambda_c}\right) \qquad (1)$$

where n_{Si} is the refractive index of silicon. For TM modes, we use the same expression, but multiply the right-hand side of Equation 1 by n_{Si}^2.[19] It has been previously been shown that WGAs have optical absorption spectra with peak wavelengths coinciding with the mode cut-off wavelengths of a HCG, and that the fractional absorption at these peak wavelengths approaches unity.[14] Figure 2f shows that for s =180 nm wide WGA pixels, the analytically calculated TE4 and TM4 cut-off wavelengths and the measured responsivity spectra peak wavelengths (for both TM and TE polarization) are in good agreement. In the following section we demonstrate that although the spectral features of the responsivities are broad in nature, with full-widths-at-half-maxima (FWHM) around 300 nm or more, it is in fact possible to reliably measure narrowband spectra across the visible range with FIN144. This is a distinct feature of the spectral reconstruction approach to microspectrometer design.[3, 22, 23, 24]

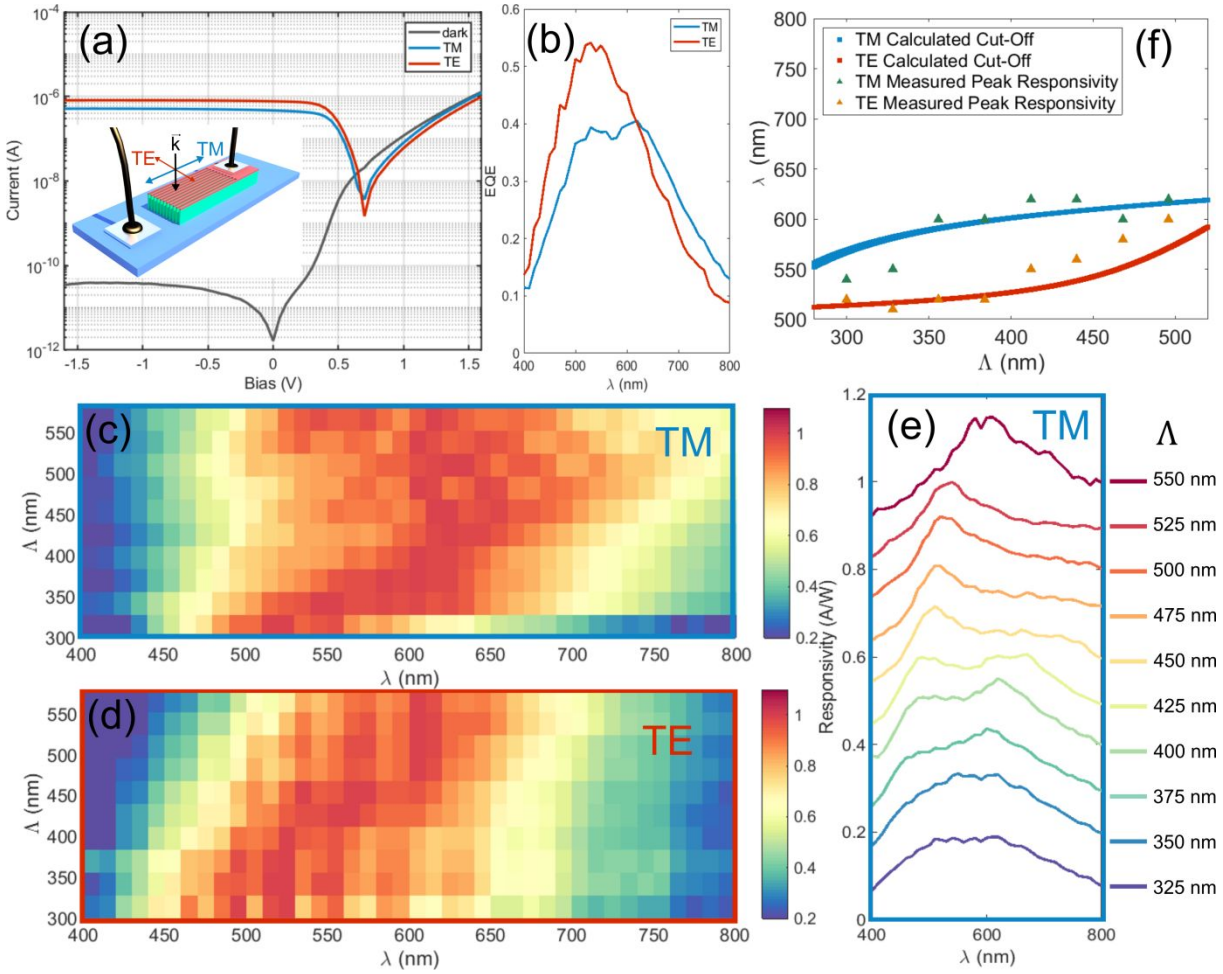

Figure 2. (a) Measured current-voltage curves of WGA pixel (s=180 nm, Λ=425 nm) in the dark (black line) and illuminated with T- (red) and TM (blue) polarized illumination (power: 18 μW, wavelength = 560 nm). Inset schematically illustrates definitions of TE and TM **(b)** Measured EQE spectra for TE (red) and TM (blue) illumination. **(c)&(d)** Measured normalized EQE spectra vs array period for 10 WGA pixels of width 180 nm under TM and TE polarized light respectively. **(e)** Measured responsivity spectra s=180 nm WGA pixels for 10 array periods (successive curves offset by 0.17 A/W for clarity). **(f)** Analytically calculated mode cut-off wavelengths, with *s*=180 nm, for TE4 (red) and TM4 (blue) WGA modes and measured peak responsivity wavelengths for TE (orange) and TM (green) polarizations.

Once the responsivity spectrum of each pixel for both polarizations is carefully measured and stored in a library, FIN144 is ready for use as a microspectrometer chip. To demonstrate the performance of our device, we first illuminate the chip with green light from our monochromator (λ=543 nm, with a FWHM of 4.8 nm). We choose a wavelength that is not used during collection of the responsivity library so as not to unduly bias the resulting spectral reconstruction. This is known as hold-out validation in machine learning. For all the sample reconstructions henceforth, we only consider narrowband spectra not found

in the responsivity library. Although our microspectrometer chip is able to measure unpolarized spectra, here we will only use TE polarized light for the following reconstructions, as we find that including photocurrent data from TM polarized light in reconstructions provides only small improvements in accuracy. Figure 3a shows the measured normalized photocurrents from each WGA pixel in FIN144, as well as the expected photocurrents found by multiplying the previously measured responsivities by the measured reference spectrum from our commercial grating spectrometer. We also plot the expected photocurrents as calculated from the measured responsivity library and the reconstructed spectrum from FIN144. All three sets of photocurrents are in good agreement, with only some small discrepancies between expected and actual photocurrents. Figure 3b shows the reference spectrum in question as well as the LASSO regularization-based estimate from FIN144. We find the agreement between the two is excellent in terms of key features such as FWHM and center wavelength, with a mean square error (MSE) of 1.3×10^{-3}. Since the test spectrum has a FWHM of 4.8 nm, we estimate FIN144 to have a spectral resolution (when measuring narrowband spectra) of 2.5 nm, which compares favorably with our reference spectrometer's stated value of 1 nm. Figure 3c shows a set of nine narrowband spectra as measured by FIN144 showing the chip is suitable for use with spectra spanning the visible range. The reference spectra can be found in the Supporting Information. To the best of our knowledge, this is the largest demonstrated operating range (423 nm to 687 nm) of a visible wavelength microspectrometer based on structurally-colored photodetectors.

Next, we evaluate the performance of FIN144 when illuminated with a naturally-occurring test spectrum. Here we pass white light through a freshly harvested bamboo leaf and measure photocurrents at each WGA pixel, as shown in the inset of Figure 3d. LASSO regularization is ill-suited to reconstructing broadband spectra,[25] so instead we use Tikhonov regularization to estimate the spectral density that minimizes the L_2 norm. Figure 3d shows the fresh bamboo leaf transmission spectrum as measured by FIN144 and by our reference spectrometer. It can be seen that these are in good agreement, with similar peak transmission wavelengths and FWHMs. The MSE between the FIN144 reconstruction and the reference spectrum is 0.0086, indicating a close match between the two as the maximum possible MSE is

unity. Finally, we test a potential 'real-world' application of our device, including confirming the temporal stability of our microspectrometer chip, calibration process and machine learning algorithm. To do this we perform spectral measurements on a freshly harvested bamboo leaf and on the same leaf after one week, without recalibrating FIN144 (that is, using the original responsivity library). Photographs of the fresh and aged leaf are shown as Figure 3e. Figure 3f and 3g show the two spectral measurements, conducted a week apart, from our reference spectrometer and from FIN144 respectively. The MSE between the FIN 144 reconstruction and reference spectrum is 0.0374. These measurements reveal that as the leaf dehydrates, its transmission reduces. The relative amplitudes of the transmission peaks a week apart are 0.18 from the reference spectra and 0.17 from the FIN144 results. This test is an important step towards a field-deployable microspectrometer, where the time evolution of the relative amplitude of spectral features can be an important indicator. For example, it can indicate water loss in vegetation on sections of farmland or rainforest. Furthermore, by comparing to previously demonstrated structural color-based visible-range microspectrometers we note that using 144 pixels (compared to 20-40[13, 14]) gives an improved match to the broadband reference spectra. The microspectrometer results here now are much closer to those of the commercial (macro) spectrometer than previously achieved, while still being many times smaller (our microspectrometer chip is only 6 mm x 6.5 mm x 0.5 mm).

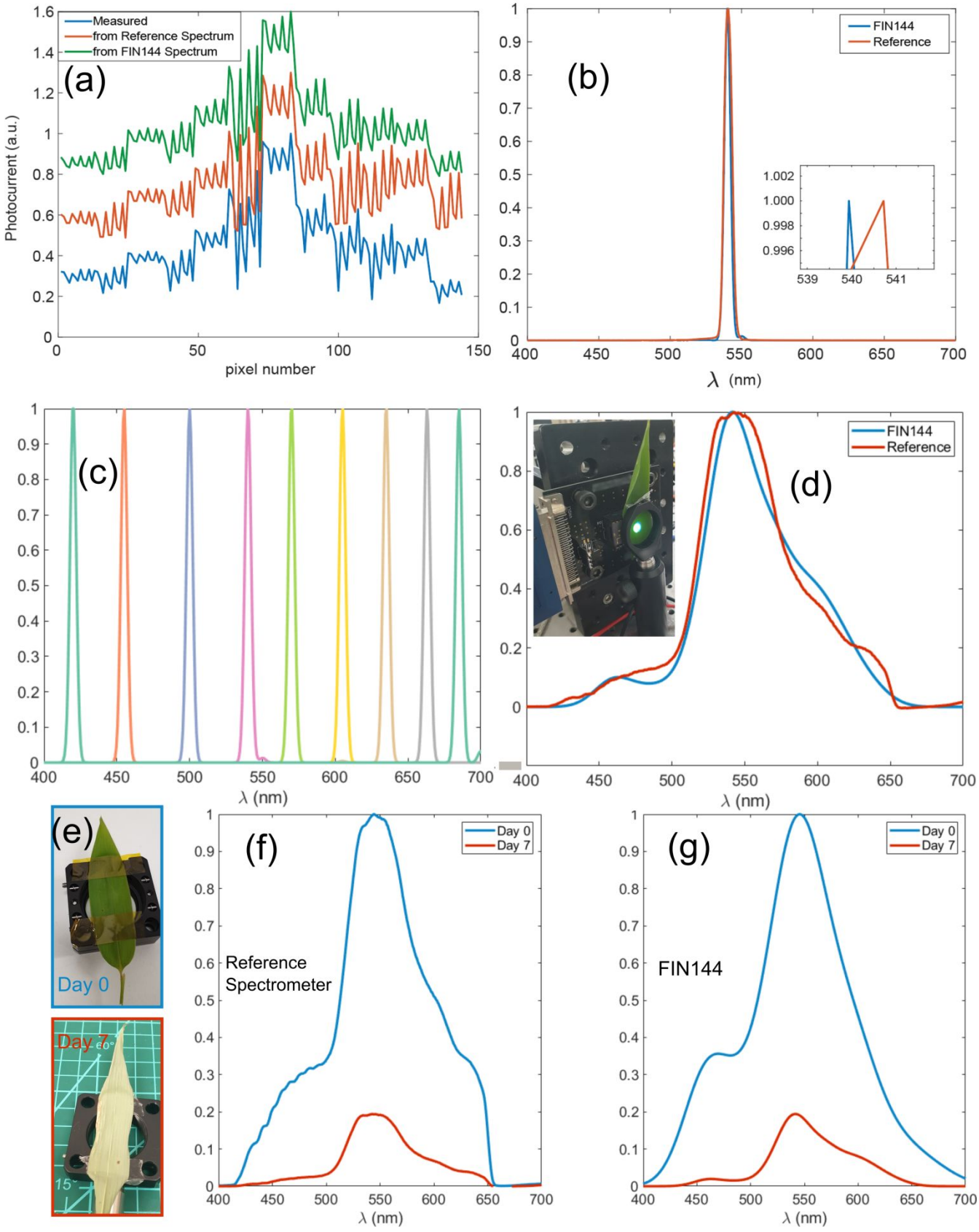

Figure 3. (a) Normalized photocurrents from all 144 WGA pixels as measured (blue line), calculated from reference spectrum (red) and calculated from FIN144 spectrum (green), for λ=543 nm narrowband test spectrum. Note that for better readability, the photocurrents are offset by 0.3 and 0.6 in the 'from

Reference Spectrum' and 'From FIN144 Spectrum' plots, respectively. **(b)** Reference (red) and reconstructed (blue) narrowband (L1) test spectrum. Inset shows the zoomed view at the peak wavelengths. **(c)** Set of reconstructed narrowband (L1) spectra, spanning the visible range. **(d)** Reconstructed (blue) and reference (red) broadband bamboo leaf transmission spectra. Inset: bamboo leaf placed in front of FIN144 for spectral measurement. **(e)** Bamboo leaves after zero (blue box) and seven (red) days since harvest. **(f)** Reference bamboo leaf transmission spectra after zero (blue) and seven (red) days. **(g)** Bamboo leaf transmission spectra as measured by FIN144 after zero (blue) and seven (red) days.

CONCLUSION

In summary, we demonstrate a visible-range microspectrometer chip comprised of 144 nanophotonic pixels, where each pixel is an array of vertically-oriented, P-I-N-doped silicon waveguides. Each WGA pixel has a unique combination of waveguide period and waveguide widths, meaning that it has a unique responsivity spectrum for both TE and TM polarizations. We show that by characterizing the latter, a responsivity library can be reconstructed that allows our device to function as a microspectrometer. The external quantum efficiencies of these pixels exceed 0.5 and are competitive with commercial silicon P-I-N photodiodes. Once characterized, photocurrent information from each pixel can be used with supervised machine learning to determine the best estimate of the spectrum illuminating the chip. We test the chip as a microspectrometer with both narrowband spectra from a monochromator and broadband spectra from a biological sample (bamboo leaf). We find our microspectrometer performs well in both cases, with an estimated resolution of 2.5 nm and with low MSE values between reference and estimated spectra across the visible range. This is enabled by judicious choice of reconstruction algorithm (i.e. L_1 or L_2 regularization). Finally, we demonstrate a potential 'real-world' application of our system by conducting bamboo leaf transmission measurements a week apart without recalibrating the responsivity library or modifying the machine learning algorithm. We find good agreement between our microspectrometer and the reference measurements. Our silicon based structurally-colored microspectrometer will suit spectroscopic applications where size, weight and power consumption are key considerations, for example in hand-held or UAV-mounted devices.

METHODS

Nanofabrication methods. To fabricate the microspectrometer chip we use the same P-I-N-I-P silicon doping structure used in Ref. [14] To define each of the 144 waveguide arrays and their pad mesas, electron beam lithography (Vistec EPBG5000+) and electron beam evaporation (IntlVac NanoChrome II) are used to create 25 nm thick Al etch masks, via polymethyl methacrylate (PMMA) lift-off. The masks protect the underlying silicon during the subsequent nano-etching step. To create high-aspect ratio (~120 nm wide, 2.7 μm tall) Si nanofeatures, a pseudo-Bosch inductively coupled plasma-reactive ion etching (ICP-RIE) recipe is used (Oxford PLASMALAB 100), although it may be possible to form these structures using metal-assisted chemical etching as well.[26] Here an etch gas chemistry at 10 mTorr of 40 sccm of SF_6 and 90 sccm of C_4F_8 is used with 1200 W ICP power and 38 W forward bias power. This recipe ensures the WGAs have smooth and vertical sidewalls, which is important for achieving the desired electrical and optical properties. We etch the silicon to the embedded *n*+ layer, so that each WGA pixel is a vertically stacked P-I-N diode. Next, direct-write photolithography (Intelligent Micropatterning SF100 XPRESS with AZ-4562 photoresist) is used to define the trenches that separate the WGA pixel rows. The trenches are etched 6.7 μm from the embedded *n*+ layer, all the way through the lower intrinsic region to the *p*+ layer below. This electrically isolates the pixel rows from one another, but pixels within a row now share a common cathode, that is, the *n*+ layer. We also etch trenches to isolate regions of the substrate where the bond pads and leads will be placed. The next step involves the atomic layer deposition (ALD, Fiji F200) of 8 nm Al_2O_3 for surface passivation of the bare silicon, which has been shown to reduce the deleterious effect of surface trap states and improve the external quantum efficiency of nanostructured silicon photodiodes.[21] Next, photolithography is used to electrically connect the WGA pixels in each column. This is done by forming SU-8 2010 epoxy "bridges" to link the pixels. We under-expose the SU-8 during UV photolithography patterning so that the corners and edges of the SU-8 bridges are rounded out and smoothed. This gives a gradual change in height from the top *p*+ pad of the WGA pixels to the wirebond pads on the *n*+ layer 2.7 μm below, instead of an abrupt step change in height which

would be problematic for metallization. The SU-8 bridges permit metallization via DC sputtering (Intlvac NanoChrome) of 250 nm Al followed by lift-off. The metal contacts atop the pad mesas also perform the function of blocking light, thereby preventing the pad mesas from contributing to the measured photocurrent. Finally, the chip is mounted in a DIP-28 chip carrier and each row pad and column pad is wire bonded (F&S Bondtech) to a unique pin in the carrier.

Characterization and Experimental Methods. The microspectrometer chip is mounted on a custom printed circuit board (PCB) with each row and column of WGA pixels connected to a single external transimpedance amplifier (SRS SR570) via a 2-channel 16-to-1 analog multiplexer integrated circuit (Analog Devices ADG726). The rows connected to one multiplexing channel, while the columns are connected to the other. The multiplexer is controlled via logic signals from an Arduino Uno connected to a PC running MATLAB. This allows us to rapidly switch the bias voltage to the desired row and column address, enabling us to measure the photocurrent from the desired WGA pixel. We measure the TE- and TM-mode responsivities of each WGA pixel by illuminating it with a known power and wavelength. Illumination is from a laser driven white light source (Energetiq EQ-99X) coupled to a monochromator (Princeton Instruments Acton SP2150). The beam is mechanically chopped (Thorlabs MC2000B) at 186 Hz with a 50% duty cycle. The polarization angle is controlled by a linear polarizer and half-waveplate (Thorlabs LPVISE100-A and AHWP05M-580). The photocurrents generated in each pixel at each illumination wavelength under a reverse bias voltage of -4.8 V are measured by a lock-in amplifier (SRS SR830). Photocurrents are collected from all 144 pixels for each wavelength and then stepped to the next wavelength by the monochromator, from 400 nm to 800 nm in steps of 5 nm. The full-width at half-maximum of light from the monochromator is measured to be less than 5 nm. After photocurrent data collection is complete, the microspectrometer chip is replaced with an optical power meter (Thorlabs PM100D, used with a 300 μm pinhole aperture) to determine the intensity spectrum illuminating the chip. Once the responsivity spectrum for each pixel is determined, the microspectrometer is ready to measure narrowband and broadband test spectra. For these measurements, the monochromator is set to

wavelengths not included in the calibration set (e.g. 573 nm) for narrowband testing. or replaced with a mirror to test broadband transmission spectra, for example, from bamboo leaves. The photocurrents generated at each pixel are measured using the multiplexing PCB, preamplifier and lock-in amplifier. For comparison of results a reference spectrum is measured for each sample using a commercial grating spectrometer (Ocean Optics QEPro).

Supervised Machine Learning Method for Spectral Reconstruction. To reconstruct the spectrum of light incident on the microspectrometer chip, the photocurrents $\boldsymbol{I}$ measured from the WGA pixels are input into a supervised machine learning algorithm, along with the *a priori* measured responsivity spectra matrix, $\boldsymbol{R}$, where $\boldsymbol{R}$ is a 144 x 81 matrix and $\boldsymbol{I}$ is a 144 x 1 vector. The reconstructed spectrum, $\boldsymbol{S}$, is the solution that minimizes the inverse problem in Equation 2, that is, it is the vector that minimizes the L_γ-norm,

$$||\boldsymbol{I} - \boldsymbol{RS}||_2^2 + \epsilon_\gamma ||\boldsymbol{S}||_\gamma^\gamma \quad (2)$$

subject to regularizer ϵ_γ, where $\gamma =$ 1 or 2. Clearly, $\boldsymbol{S}$ is a 81 x 1 vector. We detail how we increase the dimensionality of $\boldsymbol{S}$ to match that of the reference spectra (517 x 1) in the Supporting Information. For narrowband spectra, such as emission lines, L_1 regularization (which is also known as LASSO regression and is equivalent to a linear support vector machine)[27] is used, as it has been previously shown to be well suited to this sparse spectral reconstruction problem.[13] To find a suitable regularizer, ϵ_1, we use a geometric sequence of 100 candidate values from $0.01\epsilon_{1max}$ to ϵ_{1max}, where ϵ_{1max} is the largest regularizer that still gives a non-null estimate of $\boldsymbol{S}$. 6-fold cross-validation is then used to find an estimate of the spectral reconstruction's mean-square-error (MSE) for each candidate value of ϵ_1. In this case, each test and training data set corresponds to 24 and 120 WGA pixels, respectively. The value of ϵ_1 with the lowest MSE is then used as the regularizer for the narrowband spectral reconstruction. For broadband (non-sparse) spectra the LASSO method is poorly suited, so instead we use Tikhonov regularization (also known as ridge regression or weight decay) to minimize the L_2 norm. The regularizer for this method, ϵ_2, is chosen via the L-curve method.[28]

ASSOCIATED CONTENT

Supporting Information

This material is available free of charge via the internet at https://pubs.acs.org

Narrowband test spectra; Matching FIN144's dimensionality with the commercial spectrometer; Photodetector dark current measurement; Measured normalized EQE spectra photodetector; Simulated EQE spectra photodetector

AUTHOR INFORMATION

Corresponding Author

Kenneth B. Crozier - Department of Electrical and Electronic Engineering, The University of Melbourne, Victoria 3010, Australia; School of Physics, The University of Melbourne, Victoria 3010, Australia; Australian Research Council (ARC) Centre of Excellence for Transformative Meta-Optical Systems (TMOS), University of Melbourne, Victoria 3010, Australia; https://orcid.org/0000-0003-0947-001X; Email: kenneth.crozier@unimelb.edu.au

Authors

Jasper J. Cadusch - Department of Electrical and Electronic Engineering, The University of Melbourne, Parkville, Victoria 3010, Australia; https://orcid.org/0000-0002-1353-7005; Email: cadusch.j@unimelb.edu.au

Jiajun Meng - Department of Electrical and Electronic Engineering, The University of Melbourne, Parkville, Victoria 3010, Australia; School of Physics, The University of Melbourne, Parkville, Victoria 3010, Australia; Australian Research Council (ARC) Centre of Excellence for Transformative Meta-Optical Systems (TMOS), University of Melbourne, Victoria 3010, Australia; https://orcid.org/0000-0002-8883-1778; Email: jiajun.meng@unimelb.edu.au

Dandan Wen – Department of Electrical and Electronic Engineering, The University of Melbourne, Parkville, Victoria 3010, Australia; Shaanxi Key Laboratory of Optical Information Technology, School of Physical Science and Technology, Northwestern Polytechnical University, Xi'an 710129, China; https://orcid.org/0000-0001-5378-5292; Email: dandanwen@nwpu.edu.cn

Vivek Raj Shrestha- School of Physics, The University of Melbourne, Parkville, Victoria 3010, Australia. https://orcid.org/0000-0002-7731-7677; Email: vivekrajshrestha@gmail.com

ACKNOWLEDGEMENTS

Fabrication was performed in part at the Melbourne Centre for Nanofabrication (MCN) of the Australian National Fabrication Facility (ANFF).

AUTHOR CONTRIBUTIONS

J.J.C. and K.B.C conceived the idea for this work. J.J.C. performed the device design, measurements and the experimental data analysis. J.J.C., J.M., D.W., and V.R.S. performed fabrication. J.J.C. and J.M. designed the experimental set-up. All authors contributed to the writing of the manuscript.

FUNDING SOURCES

Palette, the Australian Research Council Linkage and Discovery Project schemes (LP160100959, DP180104141 and DP210103428) and the Australian Research Council Centre of Excellence for Transformative Meta-Optical Systems (Project ID CE200100010)

REFERENCES

(1) Lipson, A.; Lipson, S. G.; Lipson, H. *Optical physics*, Cambridge University Press: 2010.

(2) Cadusch, J. J.; Meng, J.; Craig, B. J.; Shrestha, V. R.; Crozier, K. B. Visible to long-wave infrared chip-scale spectrometers based on photodetectors with tailored responsivities and multispectral filters. *Nanophotonics* **2020,** *9* (10), 3197-3208.

(3) Yang, Z.; Albrow-Owen, T.; Cai, W.; Hasan, T. Miniaturization of optical spectrometers. *Science* **2021,** *371* (6528).

(4) Kurokawa, U.; Choi, B. I.; Chang, C.-C. Filter-based miniature spectrometers: spectrum reconstruction using adaptive regularization. *IEEE Sensors Journal* **2010,** *11* (7), 1556-1563.

(5) Li, E.; Chong, X.; Ren, F.; Wang, A. X. Broadband on-chip near-infrared spectroscopy based on a plasmonic grating filter array. *Opt. Lett.* **2016,** *41* (9), 1913-1916.

(6) Bao, J.; Bawendi, M. G. A colloidal quantum dot spectrometer. *Nature* **2015,** *523* (7558), 67-70.

(7) Wang, Z.; Yi, S.; Chen, A.; Zhou, M.; Luk, T. S.; James, A.; Nogan, J.; Ross, W.; Joe, G.; Shahsafi, A. Single-shot on-chip spectral sensors based on photonic crystal slabs. *Nat. Commun.* **2019,** *10* (1), 1-6.

(8) Craig, B. J.; Meng, J.; Shrestha, V. R.; Cadusch, J. J.; Crozier, K. B. Mid- to long-wave infrared computational spectroscopy using a subwavelength coaxial aperture array. *Sci. Rep.* **2019,** *9* (1), 13537.

(9) Craig, B.; Shrestha, V. R.; Meng, J.; Cadusch, J. J.; Crozier, K. B. Experimental demonstration of infrared spectral reconstruction using plasmonic metasurfaces. *Opt. Lett.* **2018,** *43* (18), 4481-4484.

(10) Meng, J.; Cadusch, J. J.; Crozier, K. B. Plasmonic Mid-Infrared Filter Array-Detector Array Chemical Classifier Based on Machine Learning. *ACS Photonics* **2021,** *8* (2), 648-657.

(11) Wang, A.; Dan, Y. Mid-infrared plasmonic multispectral filters. *Sci. Rep.* **2018,** *8* (1), 1-7.

(12) Yang, Z.; Albrow-Owen, T.; Cui, H.; Alexander-Webber, J.; Gu, F.; Wang, X.; Wu, T.-C.; Zhuge, M.; Williams, C.; Wang, P. Single-nanowire spectrometers. *Science* **2019,** *365* (6457), 1017-1020.

(13) Meng, J.; Cadusch, J. J.; Crozier, K. B. Detector-Only Spectrometer Based on Structurally Colored Silicon Nanowires and a Reconstruction Algorithm. *Nano Lett.* **2019**, 320-328.

(14) Cadusch, J. J.; Meng, J.; Craig, B.; Crozier, K. B. Silicon microspectrometer chip based on nanostructured fishnet photodetectors with tailored responsivities and machine learning. *Optica* **2019,** *6* (9), 1171-1177.

(15) Solanki, A.; Li, S.; Park, H.; Crozier, K. B. Harnessing the interplay between photonic resonances and carrier extraction for narrowband germanium nanowire photodetectors spanning the visible to infrared. *ACS Photonics* **2018,** *5* (2), 520-527.

(16) Seo, K.; Wober, M.; Steinvurzel, P.; Schonbrun, E.; Dan, Y.; Ellenbogen, T.; Crozier, K. B. Multicolored vertical silicon nanowires. *Nano Lett.* **2011,** *11* (4), 1851-6.

(17) Park, H.; Dan, Y.; Seo, K.; Yu, Y. J.; Duane, P. K.; Wober, M.; Crozier, K. B. Filter-free image sensor pixels comprising silicon nanowires with selective color absorption. *Nano Lett.* **2014,** *14* (4), 1804-1809.

(18) Li, S. Q.; Solanki, A.; Frigerio, J.; Chrastina, D.; Isella, G.; Zheng, C.; Ahnood, A.; Ganesan, K.; Crozier, K. B. Vertical Ge–Si Nanowires with Suspended Graphene Top Contacts as Dynamically Tunable Multispectral Photodetectors. *ACS Photonics* **2019,** *6* (3), 735-742.

(19) Chang-Hasnain, C. J.; Yang, W. High-contrast gratings for integrated optoelectronics. *Advances in Optics and Photonics* **2012,** *4* (3), 379-440.

(20) Fountaine, K. T.; Kendall, C. G.; Atwater, H. A. Near-unity broadband absorption designs for semiconducting nanowire arrays via localized radial mode excitation. *Opt. Express* **2014,** *22* (103), A930-A940.

(21) Juntunen, M. A.; Heinonen, J.; Vähänissi, V.; Repo, P.; Valluru, D.; Savin, H. Near-unity quantum efficiency of broadband black silicon photodiodes with an induced junction. *Nat. Photonics* **2016,** *10* (12), 777-781.

(22) Oliver, J.; Lee, W.-B.; Lee, H.-N. Filters with random transmittance for improving resolution in filter-array-based spectrometers. *Opt. Express* **2013,** *21* (4), 3969-3989.

(23) Hartmann, W.; Varytis, P.; Gehring, H.; Walter, N.; Beutel, F.; Busch, K.; Pernice, W. Waveguide‐integrated broadband spectrometer based on tailored disorder. *Adv. Opt. Mater.* **2020,** *8* (6), 1901602.

(24) Redding, B.; Liew, S. F.; Sarma, R.; Cao, H. Compact spectrometer based on a disordered photonic chip. *Nat. Photonics* **2013,** *7* (9), 746-751.

(25) Oliver, J.; Lee, W.; Park, S.; Lee, H.-N. Improving resolution of miniature spectrometers by exploiting sparse nature of signals. *Opt. Express* **2012,** *20* (3), 2613-2625.

(26) Li, X. Metal assisted chemical etching for high aspect ratio nanostructures: A review of characteristics and applications in photovoltaics. *Current Opinion in Solid State and Materials Science* **2012,** *16* (2), 71-81.

(27) Jaggi, M. *An equivalence between the lasso and support vector machines*; 0429076126; Chapman and Hall/CRC New York: 2014.

(28) Kindermann, S.; Raik, K. A simplified L-curve method as error estimator. *ETNA - Electronic Transactions on Numerical Analysis* **2020,** *53*, 217-238.

For Table of Contents Use Only

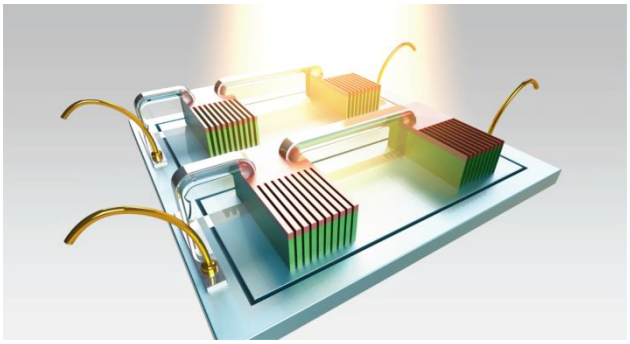

Title: Compact, Light-Weight and Filter-Free: An All-Si Microspectrometer Chip for Visible Light Spectroscopy

Authors: Jasper J. Cadusch, Jiajun Meng, Dandan Wen, Vivek Raj Shrestha and Kenneth B. Crozier

TOC graphic synopsis:

Left: Schematic illustration of the compact silicon waveguide array microspectrometer chip